ChemInform Abstract: Structural Characterization of Catalytically Active Metal Nanoclusters in Poly(amide imide) Films with High Metal Loading

5 AUTHORS, INCLUDING:

Michael Oehring

Helmholtz-Zentrum Geesthacht

64 PUBLICATIONS   1,471 CITATIONS

SEE PROFILE

Detlev Fritsch

Fraunhofer Institute for Applied Polymer Res…

100 PUBLICATIONS   3,141 CITATIONS

SEE PROFILE

Structural Characterization of Catalytically Active Metal Nanoclusters in Poly(amide imide) Films with High Metal Loading

L. Tröger,[†] H. Hünnefeld,[†] S. Nunes,[‡] M. Oehring,[§] and D. Fritsch*,[∥]

Hamburger Synchrotronstrahlungslabor (HASYLAB) am Deutschen Elektronen-Synchrotron (DESY), Notkestrasse 85, D-22603 Hamburg, Germany, Institute of Chemistry, University of Campinas, 13083-970 Campinas, SP, Brazil, Institut für Werkstofforschung, GKSS-Forschungszentrum Geesthacht GmbH, Max-Planck-Strasse, D-21502 Geesthacht, Germany, and Institut für Chemie, GKSS-Forschungszentrum Geesthacht GmbH, Max-Planck-Strasse, D-21502 Geesthacht, Germany

Noble metal clusters were generated and stabilized in poly(amide imide) (PAI) polymers in high dispersion and high concentration of typically 15 wt %. The loaded polymers were prepared as pore-free, mechanically stable membranes, which have been successfully tested for catalytic activity in membrane reactors. Pure Pd- and Ag-loaded as well as bimetallic Pd/Ag, Pd/Cu, Pd/Co, and Pd/Pb PAI films were investigated by means of X-ray absorption spectroscopy (XAFS), X-ray diffraction (XRD), and transmission electron microscopy (TEM) to characterize the structure and morphology of the metal clusters in the protective polymer. The measurements consistently show a homogeneous distribution of metallic nanoclusters of 1−3 nm size with a smaller amount of larger aggregates up to 30 nm in some of the films. The precise cluster size and distribution critically depend on the solvents used (*N*-methyl-2-pyrrolidone, tetrahydrofuran) as well as on other preparation parameters such as the stirring time of the metal precursor/polymer solution. In the case of Pd/Ag and Pd/Pb bimetallic films no clear evidence for the formation of bimetallic clusters in the membrane, i.e. alloying of both metal components, is found. In Pd/Cu and Pd/Co membranes, chlorine from the CuCl$_2$ and CoCl$_2$ precursors reacts with Pd, which may influence the Pd catalytic behavior. Reduction of the oxidized metal nanoclusters by H$_2$ at 300 K is quantitatively studied by means of XAFS and gas permeation. Optimum membrane preparation conditions are discussed with respect to the cluster formation mechanism.

Introduction

Metal clusters attract considerable interest for basic research due to their potential regarding new technologies for advanced materials and applications such as in catalysis.[1−6] Single nanoclusters may survive in high vacuum for some time, but macroscopic visible amounts of nanoclusters need to be stabilized by protective colloids: polymers,[7−9] surfactants,[10−12] or solvents.[13,14] Clearly, the protectiveness is closely related to the generation, stability, quality, and application of the clusters.

Polymer-stabilized clusters are obtainable in small sizes, in high dispersions,[8,15] and also in bimetallic quality[16,17] through generation from metal precursors by reduction in diluted solutions together with a protective polymer like poly(*N*-vinyl-2-pyrrolidone) (PVP) or polyvinyl alcohol (PVA1). This method is characterized by nonspecific interaction between precursor and polymer. Low amounts of total cluster content are achievable: typically up to 3 wt %, only. With metal complexes covalently attached to the polymer repeating unit[18] well-defined precursors after subsequent reduction may lead to clusters with adjusted size, size distribution, and spatial distribution in the polymer matrix. Depending on the polymer, the achievable metal content varies. Up to 50 wt % is possible with homopolymers,[18] but in practice and for controlled cluster properties between 3 and 15 wt % is indicated. In all cases

specially designed polymers are required: mechanical properties of the films may be poor. To overcome these restrictions, a new method was recently developed.[19,20] It simply works by adding a metal precursor to a polymer solution, after complete mixing, casting to a film, and evaporating the solvent. A final, fast reduction step forms nanoscale clusters, which are partitioned isotropically throughout the polymer matrix. The method is not limited to a special polymer but works best with polymers containing amide bonds such as poly(amide)s (PA) or poly-(amide imide)s (PAIs). Moreover, depending on the structure most PAIs maintain their toughness (highly flexible film properties) up to high percentages of 15−30 wt % metal clusters and become insoluble. These films have been proposed as membranes[20] and tested in the membrane mode for catalytic activity.[21] A few examples of catalysis using protected catalyst particles in polymer films have been reported.[22,23] Rarely were such films utilized in the membrane mode for catalysis.[24]

Other methods to form clusters in polymer films take advantage of the ability to bind cluster precursors to ionic polymers like Nafion[25,26] followed by reduction to metal clusters or use organometallics as precursors.[27] Also available are cryochemical methods to cocondensate metals and solvent vapors at liquid nitrogen temperatures, yielding solvent-stabilized clusters.[28−31] Recently, supercritical solutions of metal complexes have also been used to incorporate clusters in poly-(4-methyl-1-pentene) and poly(tetrafluoroethylene).[32] A unique, simple approach using an electrochemical method results in stabilized, soluble nanoclusters from a wide variety of metals.[33]

In this paper, the structure, size, and size distribution of noble metal nanoclusters embedded in PAI membranes are investigated. With respect to catalytic properties, both the structure and size of the metallic clusters are crucial parameters. As they depend on the preparation, the influence of preparation param-

† Hamburger Synchrotronstrahlungslabor am Deutschen Elektronen-Synchrotron.
‡ University of Campinas.
§ Institut für Werkstofforschung, GKSS-Forschungszentrum Geesthacht GmbH.
∥ Institut für Chemie, GKSS-Forschungszentrum Geesthacht GmbH.
* Corresponding author.
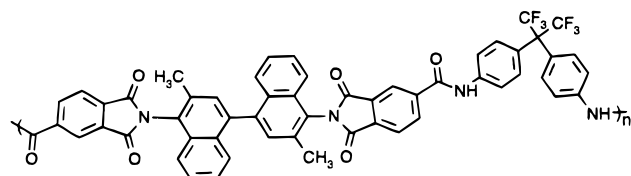⊗ Abstract published in *Advance ACS Abstracts,* February 1, 1997.

Figure 1. Structure of the poly(amide imide) polymer serving as a host for the metal nanoclusters (details in ref 20). Note the hexa-fluoroisopropylidene unit.

TABLE 1: Preparation Parameters for the Investigated Metal-Loaded Polymer Films[a]

no.	metal	polymer	metal precursor	solvent/stirring time
1	Pd	PAI	$PdAc_2$	NMP/1.5 h
2	Pd	PAI	$PdAc_2$	NMP/3 h
3	Pd	PAI	$PdAc_2$	NMP/5 h
4	Pd	PAI	$PdAc_2$	NMP/16 h
5	Pd	PAI	$PdAc_2$	THF/1 h
6	Pd	PAI	$PdAc_2$	THF/16 h
7	Pd	silicone	$PdAc_2$	THF/1 h
8	Ag	PAI	$AgBF_4$	NMP/1 h
9	Ag	PAI	$AgBF_4$	NMP/3 h
10	Pd/Ag(1:9)	PAI	$PdAc_2$, $AgBF_4$	NMP/2 h
11	Pd/Ag(3:1)	PAI	$PdAc_2$, $AgBF_4$	NMP/3 h
12	Pd/Ag(3:1)	PAI	$PdAc_2$, AgAc	NMP/4 h
13	Pd/Pb(1:1)	PAI	$PdAc_2$, $PbAc_2 \cdot 3H_2O$	NMP/16 h
14	Pd/Pb(9:1)	PAI	$PdAc_2$, $PbAc_2 \cdot 3H_2O$	NMP/2 h
15	Pd/Cu(1:1)	PAI	$PdAc_2$, $CuCl_2 \cdot 2H_2O$	NMP/4 h
16	Pd/Cu(1:1)	PAI	$PdAc_2$, $CuCl_2 \cdot 2H_2O$	NMP/16 h
17	Pd/Cu(3:1)	PAI	$PdAc_2$, $CuCl_2 \cdot 2H_2O$	NMP/16 h
18	Pd/Cu(9:1)	PAI	$PdAc_2$, $CuCl_2 \cdot 2H_2O$	NMP/2 h
19	Pd/Cu(9:1)	PAI	$PdAc_2$, $CuCl_2 \cdot 2H_2O$	NMP/16 h
20	Pd/Co(9:1)	PAI	$PdAc_2$, $CoCl_2 \cdot 6H_2O$	NMP/2 h

[a] PAI denotes the polymer structure shown in Figure 1. Ac = acetate. Metal loading of all films is 15 wt %. Reduction is performed in all cases by means of $MeOH/NaBH_4$ (see text).

eters is also discussed. Both monometallically loaded (Pd, Ag) and bimetallically loaded membranes (Pd/Ag, Pd/Cu, Pd/Co, Pd/Pb) are studied. In the latter ones, interaction of the individual components, e.g. metal alloying and choice of precursors, is discussed.

Experimental Section

Chemicals. Solvents used were of analytical grade or highest purity available and obtained from Merck. Palladium acetate was received from Fluka. Cobalt(II) chloride hexahydrate, copper(II) chloride dihydrate, lead(II) acetate trihydrate, silver acetate, silver tetrafluoroborate, and sodium borohydride all were from Merck. The cluster-stabilizing polymer was a proprietary, highly gas permeable poly(amide imide) synthesized in our laboratory.[34] The structure is given in Figure 1.

Preparation of Polymer Film Embedded Clusters. Solutions were prepared by solving the polymer and the metal precursor separately in the desired concentrations, mixing of the solutions, and further stirring for 1−16 h, as specified in Table 1. Films were formed from ∼10 wt % tetrahydrofuran (THF) or *N*-methylpyrrolidone (NMP) solutions by casting to horizontally adjusted, hydrophobic glass plates and evaporating the solvent by (i) a weak argon sweep in a closed chamber at room temperature overnight (THF) or (ii) at 80 °C on a heating plate freely in air overnight (NMP). The films were peeled off the plate and soaked in a freshly prepared methanol−sodium borohydride solution for 15 min. Upon dipping, the brown color of the film immediately turned to black (Pd and Pd−metal mixtures) or silvery-blackish (Ag). Washing with methanol and drying in vacuum (110 °C; overnight below 1 mbar) results in

solvent- and pore-free films of 40−50 μm thickness containing nanoscale metal clusters. Pore-freeness of the membranes was checked by testing for gas selectivity. Porosities $>10^{-8}$% would result in a significant decrease in selectivity.[35] The clusters are distributed uniformly throughout the film as checked by electron microscopy. Metal contents from 0 to 30 wt % are achieved with only little effect on the mechanical properties. For comparability, all films studied in this paper contain 15 wt % metal. They are no longer soluble in THF or NMP.

Gas Permeation and Redox Behavior. Permeability and diffusivity measurements were carried out at 30 °C with a self-built time-lag vacuum apparatus fitted with two MKS Baratron sensors (10 mbar, 5 bar) and controlled by computer. The probed membrane area was 13.2 cm^2. Feed pressure varied from 300 mbar to 1 bar. Permeate pressure was $<10^{-3}$ mbar in the beginning and was recorded up to 1−10 mbar, depending on the feed gas. Evacuation time was set to at least six time lags. Permeability *P* was calculated from the slope in the steady-state region, and apparent diffusion coefficient D_a from the time lag Θ by $D_a = l^2/6\Theta$, where *l* is the film thickness. Apparent solubility coefficient S_a was calculated by $S_a = P/D_a$. Information on the redox behavior of the metal-loaded membranes was obtained from alternating hydrogen and oxygen permeation experiments. Feed gases were not changed directly from hydrogen to oxygen (and vice versa), but intermediate flushing with an inert gas (helium or nitrogen) was always employed.

Transmission Electron Microscopy. For transmission electron microscopy, samples were cut with a diamond knife at about −50 °C in a Reichert Jung Ultracut-S/FC4E Cryo-ultramicrotome, collected on 400 mesh copper grids, and observed in a Zeiss CEM-902 transmission electron microscope, working at 80 kV. A magnetic mirror/prism system was used to select only elastic electrons and improve contrast.

X-ray Diffraction. X-ray diffractograms were taken with a Siemens D5000 $\Theta-\Theta$ diffractometer using Cu radiation and a graphite secondary monochromator. Measurements were performed in reflection and transmission geometry at room temperature from unsupported membranes or membranes mounted on an acrylic glass to reduce the effects of the waviness of thin membranes. Both detection geometries yielded identical results with respect to the metal components with small differences in the background function.

X-ray diffraction peaks of the metallic components were fitted by means of double pseudo-Voigt lines which describe the Cu $K\alpha_1, K\alpha_2$ doublets. From the fits, the position and width of the reflections were obtained. The lattice parameters of the corresponding metal phases were determined from the peak positions. In most cases, metal diffraction peaks consist of a sharper and a broader component, which can be assigned to clusters of different size. From the widths of the reflections, grain sizes of the reflecting grains were calculated. Following the method of Williamson and Hall,[36] effects of internal strain on the width of the reflections were generally found to be insignificant. Grain sizes *L* therefore were obtained from the Scherrer equation[37,38]

$$L = 0.9 \frac{\lambda}{\Delta(2\Theta) \cos \Theta} \qquad (1)$$

where $\lambda = 1.5406$ Å is the wavelength of the Cu $K\alpha_1$ radiation, Θ the diffraction angle, and $\Delta(2\Theta)$ the full reflection width in radians, which has been corrected for the instrumental broadening and the wavelength width of the $K\alpha$ line.

X-ray Absorption. XAFS experiments measuring the local environment around the metal atoms in the membranes were performed at the Hamburger Synchrotronstrahlungslabor (HA-

Metal Nanoclusters in PAI Films

J. Phys. Chem. B, Vol. 101, No. 8, 1997 **1281**

SYLAB) at the Deutsches Elektronen-Synchrotron (DESY), Hamburg, Germany. The spectra were taken at beamlines X1.1 and E4 of the positron storage ring DORIS III. They are equipped with Si(311) and Si(111) double-crystal monochromators covering the photon energy ranges 10−30 and 3−10 keV, respectively. A typical primary photon flux at the sample was approximately 10^9 photons s^{-1} mm^{-2}. Absorption spectra were taken in conventional transmission setup. The ionization chambers were filled with pure nitrogen or argon gas or an appropriate mixture of both that yields an absorption of about 10% in the first and 30% in the second ionization chamber. Simultaneously to the sample spectra, reference metal spectra were taken using a third ionization chamber. EXAFS scans were measured over an energy range of 1000−2000 eV with a counting time of 1−2 s/point and a resolution of 2−5 eV. Higher harmonics were reduced by piezo detuning of the first monochromator crystal with a feedback system to about 60% of the maximum Bragg peak intensity. The size of the X-ray beam on the sample was about 0.3 × 6 mm^2.

XAFS spectra were measured at the K-edges of all metal atoms in each of the films (Pd, Ag, Pb, Cu, Co). Depending on the X-ray energy of the particular absorption edge, between two and 10 of the 50 μm thick membranes were stacked on top of each other to reach an optimum thickness for the transmission setup of about $\mu_{tot}d \cong 1$. Scanning of the X-ray beam across the samples showed no changes in the measured XAFS signals, i.e. a great homogeneity expected from the pore-freeness of the membranes. Generally, the spectra were of high quality, exhibiting high signal-to-noise ratios. Measurements were performed at 300, 80, and/or 20 K using liquid nitrogen and liquid helium cryostats. At 300 K, samples could be held in a H$_2$ gas stream (atmospheric pressure) for typically 45 min in a special sample holder and were measured under this condition. This way, the reduction behavior of the membranes at room temperature was studied.

Quantitative XAFS data evaluation employed the programs AUTOBK (background subtraction) and FEFFIT (Fourier transformation and fitting) from the University of Washington package.[39] Experimental EXAFS data were analyzed in distance space by means of multiple-shell fits using the cumulant expansion method.[40,41] Theoretical standards for scattering phases and amplitudes of the photoelectron wave were obtained from the ab initio multiple scattering code FEFF5.[42] By means of the analysis of metal and metal oxide reference spectra the number of fitting parameters could be reduced (see below).

In the case of monometallic, Pd-loaded membranes the variables and parameters used in the fits were as follows. The experimental EXAFS spectra were Fourier transformed in the range $k = 3.0-12.9$ Å^{-1} of the photoelectron wavenumber using a k^2 weighting. Quantitative fitting of the Fourier transforms (FT) was performed by means of two-shell fits in the range $r = 1.0-3.1$ Å. This range covers the two dominant peaks seen in the FT of all the spectra, which are identified as Pd−O and Pd−Pd shells and correspond to an oxidized and metallic fraction of the clusters, respectively. Six variables were used in the two-shell fits: mean coordination numbers n(Pd−O) and n(Pd−Pd), mean interatomic distances R(Pd−O) and R(Pd−Pd), and mean-square relative displacements between the atoms σ^2(Pd−O) and σ^2(Pd−Pd). By analyzing the first shell around Pd in reference spectra of bulk PdO and metallic Pd foil in the same way as the membrane spectra, the energy shifts ΔE_0 of the photoelectron energy zero were fixed to the reference values of ΔE_0(Pd−O) = 10.39 eV and ΔE_0(Pd−Pd) = 3.77 eV. Also, the multielectron reduction factors were determined as S_0^2(Pd−O) = 0.791 and S_0^2(Pd−Pd) = 0.839, respectively. It was

checked that asymmetries of the radial pair distribution function of the Pd−O and Pd−Pd shells, which were introduced in the fits, did not improve the quality of the fits significantly. Therefore, cumulants higher than the second one were not included as fitting parameters, although it is known that for small particles they can have important effects, e.g. at higher temperatures.[43] Two-shell fits performed in this manner were generally very well defined since the information content of the data corresponds to about 12 fitting parameters.[40] For all Pd monometallic films, the experiment was very well described by the fit.

Bimetallic membranes were analyzed analogously to the Pd monometallic ones (for Pd and also for the other atom species). In some cases of bimetallic films, e.g. for Pd/Cu films, the XAFS experiments could not be well described by the results of two-shell fits. In these cases, an additional third shell was included, namely, Pd−Cl, which models a metal metal-precursor interaction. Good agreement of three-shell fits with the experimental results was then obtained.

Onion Model. Mean interatomic distances and mean-square relative displacements obtained from the XAFS analysis are easily interpreted (see below). In addition, the mean coordination numbers obtained from the fits carry important structural information of the clusters in two aspects. In this section, we only consider monometallically Pd-loaded membranes. Others are treated analogously. First, n(Pd−O) and n(Pd−Pd) are dependent on the fractions of oxidized and metallic Pd in the membrane. Secondly, in small clusters mean coordination numbers are reduced due to the increasing cluster surface contribution. Therefore, oxide and metal phase fractions as well as particle sizes can be determined by means of the following simple model.

The metal particles in the membranes are assumed to be of spherical shape and to consist of a metal core and an oxidized surface layer; see figure in the Appendix (*onion model*). Secondly, it is assumed that all metal clusters in the membrane have the same well-defined size of diameter D. Certainly, the actual cluster sizes will be distributed around a mean value or will be of even more complicated form. In this case the size D expresses an effective mean cluster size in which the actual cluster sizes are weighted according to their total mass.

Pd atoms in the oxidized phase do not have Pd nearest neighbors and therefore only contribute to the first peak Pd−O in the FT. Accordingly, metallic Pd only contributes to the second FT peak Pd−Pd. The observed XAFS coordination numbers n(Pd−O) and n(Pd−Pd) are therefore reduced from their bulk values of 4 and 12, respectively, by the amount of which each of the phases is present in the membrane. In addition, small clusters have a significant number of surface atoms with a reduced nearest neighbor coordination. Dependent on the cluster size, mean coordination numbers are therefore further reduced. In the onion model, the experimentally observed XAFS coordination numbers n(Pd−O) and n(Pd−Pd) are given as

$$n(\text{Pd}-\text{O}) = 4f_{\text{O}}^{\text{ring}}(d,l_{\text{ox}})[1 - p(d,l_{\text{ox}})] \qquad (2)$$

$$n(\text{Pd}-\text{Pd}) = 12f_{\text{Pd}}(d)\, p(d,l_{\text{ox}}) \qquad (3)$$

where d denotes the diameter of the metal core of the cluster, l_{ox} is the thickness of the oxide layer, $D = d + 2l_{\text{ox}}$ is the full cluster diameter, $p(d,l_{\text{ox}})$ is the percentage of Pd atoms in the metallic phase in these clusters (referred to as the total amount of Pd), and $f_{\text{O}}^{\text{ring}}(d,l_{\text{ox}})$ and $f_{\text{Pd}}(d)$ are normalized mean coordination numbers taking into account surface effects in the
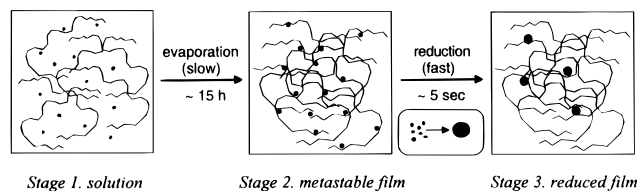
Figure 2. Proposed formation mechanism of nanoclusters. Stage 1: molecular, isotropic partition of metal salt precursor and polymer chains in solution. Possible chelate formation. Stage 2: molecular, isotropic partition of metal salt precursor throughout the polymer supported by chelate formation with amide/imide groups. Minor amounts of solvent present (5−10%). Stage 3: isotropic (statistical) partition of nanoclusters in the polymer matrix. The nanoclusters are chemisorbed onto the polymer chain.

oxide layer ring and the metal core, respectively. The latter functions vary between 0 and 1. Their detailed form is given in the Appendix. By use of eqs 2 and 3, from a pair of experimentally determined values $n(Pd-O)$ and $n(Pd-Pd)$ the corresponding cluster diameter D and the oxide layer thickness l_{ox} are directly calculated.

Results and Discussion

Proposed Cluster Formation Mechanism. The proposed formation mechanism of nanoclusters is given in Figure 2. After thorough mixing, a homogeneous distribution of precursor metal salt in the polymer solution is achieved (stage 1). Casting of this solution to a glass plate and slow evaporation of the solvent for about 10−15 h yields a metastable membrane film (stage 2). The color of the film depends on the applied precursor salt. In any case transparent films containing around 5% of residual solvent result. These films are metastable because dipping into methanol or water for some hours leads to almost complete washing out of the precursor salt. In contrast, by dipping into a NaBH$_4$/methanol solution, within seconds the color of the film changes, e.g. from brown to black for palladium acetate-containing films. During this fast reduction step (stage 3) the polymer-solved metal precursor is reduced to free metal. Reduced Pd films prepared from NMP (specular, black) differ in appearance from their analogues prepared from THF (specular, silvery). No washing out of the noble metals was observed during the reduction step. Under the applied conditions, only copper, nickel, and manganese salts showed some bleeding into the solution, visible by the turbidity formed by dark microscopic particles in solution and on top of the film. At the beginning of reduction stage 3, the polymer is somewhat swollen by residual solvent and methanol from the reducing bath. Single atoms of metals are able to diffuse inside the dry polymers with low diffusion coefficients.[44] In swollen polymers diffusion processes will increase significantly. Therefore, single metal atoms will be able to combine to clusters. The final clusters are chemisorbed to the polymer chains because the membrane film, after stage 3 (Figure 2), becomes completely insoluble in solvents used for poly(amide imide). During the reduction step a shrinking of the film by 5−10% in diameter was observed. This is probably due to washing out of some residual solvent and reduced volume of the metallic particles compared to the salt, e.g. palladium acetate to Pd.

Attempts to classify the nature of the metal cluster interaction with the polymer by means of infrared (IR) spectroscopy were not successful. However, changes near the amide II bond at 1520 cm^{-1} were observed for Pd-cluster-containing films. Compared to the pure polymer, the absorbed IR intensity of normalized spectra increases (at 1411 cm^{-1} from 0.54 to 0.72, at 1462 cm^{-1} from 0.25 to 0.42, at 1575 cm^{-1} from 0.2 to 0.5).

TABLE 2: N$_2$ Diffusivities $D_a(N_2)$, Solubilities $S_a(N_2)$, and Permeabilities $P(N_2)$ of Selected Membranes^a

film		$D_a(N_2)$	$S_a(N_2)$	$P(N_2)$
	pure PAI	1.59	16.2	2.50
8	Ag	0.96	17.2	1.64
10	Pd/Ag(1:9)	0.96	17.0	1.63
14	Pd/Pb(9:1)	1.37	16.9	2.32
18	Pd/Cu(9:1)	0.94	17.1	1.61

^{a} D_a in 10^{-8} cm^2/s, S_a in 10^{-3} cm^3(STP)/(cm^3 cmHg), P in Barrer $= 10^{-10}$ cm^3(STP) cm/(cm^2 s cmHg). Error bars of these quantities are about 10%.

TABLE 3: H$_2$ Diffusivities $D_a(H_2)$ and Solubilities $S_a(H_2)$ of Selected Membranes^a

film		Pd content/wt %	$D_a(H_2)$	$S_a(H_2)$
3	Pd	15.0	0.48	1100.0
20	Pd/Co(9:1)	13.5	0.89	520.0
18	Pd/Cu(9:1)	13.5	1.70	320.0
14	Pd/Pb(9:1)	13.5	2.9	240.0
12	Pd/Ag(3:1)	11.3	2.1	230.0
10	Pd/Ag(1:9)	1.5	65.0	12.0
8	Ag	0.0	200.0	3.5
	pure PAI	0.0	300.0	3.4

^{a} D_a in 10^{-8} cm^2/s, S_a in 10^{-3} cm^3(STP)/(cm^3 cmHg).

Gas Permeation and Redox Behavior of Nanoclusters. Diffusivity and permeability of cluster-containing membranes decrease for gases nonreactive to the metal clusters compared to pure polymer membranes. This is in accordance with membranes comprising inorganic fillers.[45] The clusters act as a diffusion barrier. They may also decrease the free volume or influence the free volume partition inside the polymer. Table 2 reports nitrogen diffusivity, solubility, and permeability data for selected membranes. Diffusivity and therefore permeability decrease by about 30% in membranes 8, 10, and 18. The solubility does not change within the experimental error. Slightly lower changes found in membrane 14 may be due to uncertainties in the measurement of the membrane thickness.

Hydrogen is expected to reduce oxidized palladium and to solve in metallic Pd clusters. Because hydrogen diffusion through the pure polymer is fast (time lags of a few seconds), these processes can only be detected if the uptake of H$_2$ in the clusters is faster than its diffusion through the membrane. Table 3 shows the results of time-lag measurements of air-stored membranes with H$_2$ feed gas. With increasing Pd content the apparent diffusivity D_a decreases up to 2 orders of magnitude, accompanied by a similar increase of apparent solubility S_a. This is the effect of H$_2$ uptake due to Pd−O reduction and solvation of hydrogen in the Pd clusters. Consistently, H$_2$ time-lag measurements performed after prolonged evacuation time on H$_2$-treated, reduced membranes show lower apparent solubilities and higher diffusivities. Ag clusters in the membrane show only very little change, as they do not solve H$_2$ at the applied temperature (30 °C).

Table 4 summarizes the results of O$_2$-permeation experiments of air-stored as well as H$_2$-treated membranes. H$_2$-treated membranes were flushed with inert He gas before O$_2$ feed. The measured apparent diffusivity and solubility reflect the oxidation behavior of the metal clusters in the membranes. The larger the Pd metal content, the larger the decrease in apparent diffusivity and, respectively, the increase in apparent solubility after H$_2$ treatment, because oxygen is consumed to oxidize the surface of the Pd clusters or possibly reacts with strongly chemisorbed H$_2$ in the clusters. Again, these processes are faster than the diffusion of O$_2$ through the polymer membrane, as they are measurable by time-lag experiments. Catalytic properties

Metal Nanoclusters in PAI Films

J. Phys. Chem. B, Vol. 101, No. 8, 1997 **1283**

TABLE 4: O$_2$ Diffusivities D_a(O$_2$) and Solubilities S_a(O$_2$) of Selected Membranes after Storing in Air and Treating with H$_2$[a]

|	film	D_a(O$_2$) after air	S_a(O$_2$) after air	D_a(O$_2$) after H$_2$	S_a(O$_2$) after H$_2$
3	Pd	3.2	23	0.19	350
20	Pd/Co(9:1)	3.0	18	0.13	260
18	Pd/Cu(9:1)	4.1	22	0.48	160
14	Pd/Pb(9:1)	5.8	25	1.1	120
12	Pd/Ag(3:1)			1.1	130
10	Pd/Ag(1:9)	4.3	20	2.7	33
8	Ag	4.3	21	4.3	21
	pure PAI	7.1	16	7.1	16

[a] D_a in 10^{-8} cm^2/s, S_a in 10^{-3} cm^3(STP)/(cm^3 cmHg).
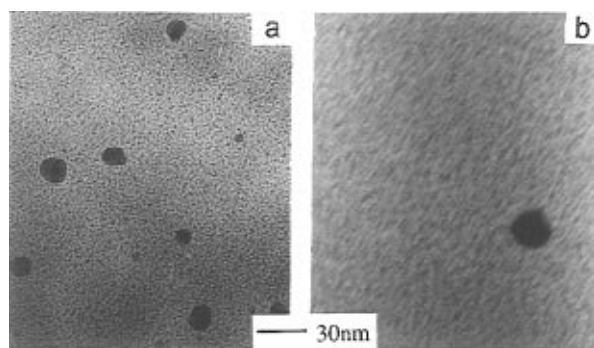
Figure 3. TEM pictures of Pd membranes prepared in NMP: (a) membrane 2, stirred for 3 h; (b) membrane 3, stirred for 5 h.
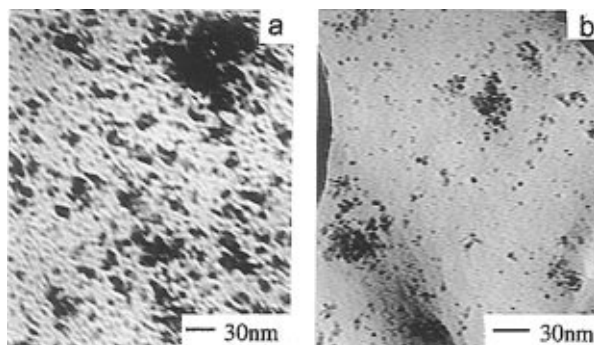
Figure 4. TEM micrographs of Pd-loaded membranes prepared in THF: (a) membrane 5, stirred for 1 h; (b) membrane 6, stirred for 16 h.

of selected membranes with respect to reduction of nitrous oxide by H$_2$ are discussed in detail in ref 21.

Cluster Size Distributions in Monometallically Loaded Membranes. Figure 3a shows the TEM picture of membrane 2. As the major component, a large amount of small clusters of size around 1 nm can be identified. In addition, a few larger particles with diameters of 5−20 nm are present. Depending on the specific membrane preparation, sizes and distribution vary. Figure 3b shows a TEM picture of membrane 3. A comparison of both TEM pictures of Figure 3 may indicate that a longer stirring time of the metal salt precursor/polymer solution reduces the amount of large particles in the membrane. This is supported by the TEM of sample 1, stirred for 1.5 h only and not shown here, which contains an even larger amount of bigger particles. However, stirring for longer than 5 h does not improve the dispersion further. Generally, the effect of stirring time is small in NMP solutions. It is more pronounced in membranes prepared from THF solutions, as seen in Figure 4, comparing membranes 5 and 6. In membrane 5, large agglomerates are present, showing that 1 h is not enough for a suitable dispersion of PdAc$_2$. Longer stirring of 16 h in membrane 6 improves
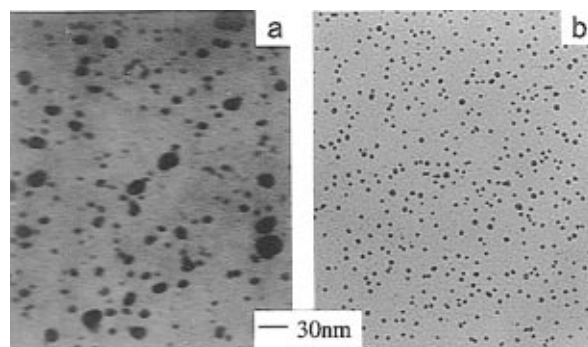
Figure 5. TEM micrographs of Ag-loaded membranes prepared in NMP: (a) membrane 8, stirred for 1 h, (b) membrane 9, stirred for 3 h.
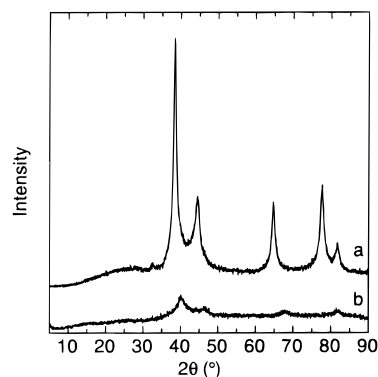
Figure 6. XRD patterns of (a) Ag-loaded membrane 8 and (b) Pd-loaded membrane 1. Spectrum b is vertically shifted against spectrum a to the extent to which the background functions above $2\Theta = 50°$ differ.

the dispersion. Generally, however, NMP appears to be a more convenient solvent to obtain a better dispersion. Interestingly, also the form of aggregation is different in NMP and THF. In NMP, well-dispersed Pd particles of small size are obtained, but a few larger dense and isolated particles are also present. In THF, aggregates are more frequent and are clearly formed by smaller particles close to each other, but not completely forming dense, large particles. The appearance of the surface differs in accordance with these findings. From THF preparations, specular, silvery membrane surfaces are obtained, whereas specular, black surfaces result from NMP.

Figure 5 shows that also for Ag-loaded membranes prepared in NMP the effect of stirring time is evident, comparing samples 8 and 9 after 1 or 3 h stirring. No aggregates, only small particles, are observed in membrane 9 after 3 h stirring. In contrast, large aggregates can be seen in sample 8. Table 5 lists mean particle sizes obtained from the TEM pictures.

Figure 6 shows diffractograms of the Pd-loaded membrane 1 and the Ag-loaded membrane 8, which reveal diffraction peaks lying at about the positions of pure fcc Pd and Ag bulk, respectively, but are broadened due to small cluster sizes in the membranes. The background functions in Figure 6 are well reproducible above $2\Theta = 50°$. The amorphous structure of the polymer mainly contributes to the background at smaller scattering angles. Most of the diffractograms resemble that of membrane 1, exhibiting weak and broadened peaks only. In addition, in most cases the broadened, strongest peaks are superimposed by even broader peaks, as is found by peak fitting. In Figure 7 the fit of the XRD peaks around $2\Theta = 40°$ is shown for membrane 2, containing only pure Pd as the metal component. Both relatively sharp and very broad peaks are lying at the angular position of the bulk Pd(111) reflection.
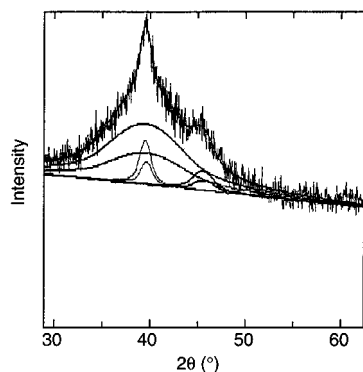
Figure 7. Fit of X-ray diffraction peaks recorded on Pd-loaded membrane 2 as a sum of very broad and relatively sharp contributions corresponding to smaller and larger clusters, respectively. Due to the Cu $K\alpha_1, K\alpha_2$ splitting, each of the contributions is fitted with a $K\alpha_1, K\alpha_2$ doublet.

The very broad diffraction peaks observed on almost all membranes exhibit peak widths of 6−13°, which are typical for those found on amorphous materials. However, elementary amorphous metals crystallize already at cryogenic temperatures.[46,47] In agreement with the results obtained by XAFS and gas permeation, the very broad diffraction peaks are therefore interpreted to be caused by small crystalline metallic clusters. From the peak widths, mean grain sizes of $L \approx 44$ Å and $L \approx 9$ Å are obtained for the relatively sharp and the very broad diffraction peaks displayed in Figure 7 for membrane 2, respectively.

As an important result of the XRD analyses, it is observed that the metal loading of the membranes consists of nanometer-sized clusters in their metallic form (fcc structure). In addition, in most of the films a bimodal cluster size distribution is concluded from the XRD spectra. This is in agreement with the observations from the TEM micrographs. Table 5 summarizes the cluster sizes in monometallically loaded membranes calculated from the Scherrer equation. Entries in italics denote minority components.

Figure 8a shows the measured Pd K-edge EXAFS signal for membrane 3. The corresponding Fourier transform (FT) reflecting the *average* radial distribution function around all Pd atoms across the X-ray beam is given in Figure 8b. The two main peaks seen around $r = 1.5$ Å and $r = 2.5$ Å are originating from Pd−O and Pd−Pd nearest neighbor distances in the sample, i.e. oxidized and metallic palladium, respectively. The distances seen in the FT are lower than the crystallographic distances due to the effect of the scattering phase.[40]

As discussed in the Experimental Section, two-shell fits of the XAFS FT yield structural parameters of the clusters. For Pd membrane 3 measured at 80 K (Figure 8) nearest neighbor distances of $R(Pd-O) = 2.03(3)$ Å and $R(Pd-Pd) = 2.75(2)$ Å, mean coordination numbers of $n(Pd-O) = 2.5(2)$ and $n(Pd-Pd) = 1.6(2)$, and mean-square relative displacements (MSRD) of $\sigma^2(Pd-O)$ (80 K) = 0.004(2) Å^2 and $\sigma^2(Pd-Pd)$ (80 K) = 0.004(1) Å^2 are obtained. The above nearest neighbor distances are in agreement with the values of tetrahedral Pd in palladium oxide, PdO, (2.02 Å) and Pd−Pd in fcc Pd (2.75 Å).[48] This demonstrates that Pd is present in the membranes in both the metallic and oxidized form. For all investigated Pd-loaded samples, nearest neighbor distances agree with these bulk values within experimental accuracy. MSRDs vary with temperature, as they originate from static *and* dynamic contributions. Observed peak heights in the FT are influenced by both MSRDs and mean coordination numbers. Variations of the MSRDs occur in different membranes and preparations, but no pro-

nounced effects are observed. Assuming the onion model, eqs 2 and 3, the above mean coordination numbers are linked to the mean cluster diameter $D = 13(2)$ Å and mean thickness $l_{ox} = 2.4(4)$ Å of the oxide surface layers in membrane 3.

Table 5 shows measured XAFS coordination numbers and the average cluster sizes D and oxide layer thicknesses l_{ox} determined from the XAFS experiments. Due to different dynamic contributions, MSRDs determined at 300 K are different from the ones at 80 K (not included in Table 5), but for all investigated samples, coordination numbers measured at both temperatures and therefore the structural parameters D and l_{ox} are identical. As an example, measurements at both temperatures are included in Table 5 for membrane 3. For all other samples, when measured at both temperatures, only 80 K measurements are listed, because the reduced MSRDs at 80 K compared to 300 K increase the accuracy in coordination number determination.

Figure 9 demonstrates the effect of H$_2$ reduction of membrane 2. Reduction was performed at 300 K over a period of 45 min using continuous H$_2$ gas flow around the fully mounted stack of membranes ready for XAFS measurement. In the XAFS spectra (Figure 9a,b) and in the Fourier transforms (Figure 9c,d), H$_2$ reduction increases the high-frequency component corresponding to the Pd−Pd peak in the FT at the expense of the lower frequency component (first peak, Pd−O contribution). As seen in Table 5, the total diameter D of the clusters remains the same, but the thickness l_{ox} of the oxide layer is reduced by about a factor of 2. A similar reduction behavior is also seen in other membranes. It is pointed out that the parameters D and l_{ox} are mean or effective quantities that average over the entire ensemble of cluster sizes and therefore should not be transferred without special care to a microscopic picture.

The agreement of cluster sizes in the membranes in Table 5 determined by the different structural methods is very convincing considering that the techniques do not probe identical properties and portions of the entire cluster ensemble. For example, the grain sizes measured by XRD correspond to the size of the metal cores of the clusters and are therefore systematically lower than the particle diameters determined by TEM and XAFS, which include the surface oxide layers as well. Naive calculations applying eq 6 in the Appendix yield approximate numbers of atoms per cluster. For example, in clusters with diameters of 3, 2, and 1 nm the number of atoms within the cluster decreases from ~960 to ~290 and ~36, respectively.

Metal−Metal Interaction in Bimetallically Loaded Membranes. To increase variety and functionality in catalytic behavior, e.g. for design of multicomponent catalysts, it is of some interest to achieve metal loading of the membranes by more than one metal species. Particularly, bimetallic clusters are favored for application. The simple preparation routine of the metal-loaded membranes easily allows the manufacture of multicomponent membranes. A number of different bimetallically loaded membranes with different mass ratios of the two incorporated metals were investigated by means of structural methods (see Table 1).

Figure 10 shows TEM pictures of the Pd/Ag membranes 11 and 12, prepared in NMP from different metal precursors. The observed cluster morphology is quite similar as that in the Pd-loaded films (previous section). A majority of nanometer-sized clusters as well as some larger clusters or aggregates are seen. However, in membrane 11, aggregation of smaller clusters to bigger agglomerates up to about 8 nm is observed, whereas in membrane 12 only scattered particles with diameters around 40 nm are present (not shown in Figure 10b). Because of quite similar stirring times in NMP, this is likely the effect of the

Metal Nanoclusters in PAI Films

J. Phys. Chem. B, Vol. 101, No. 8, 1997 **1285**

TABLE 5: Mean Cluster Sizes in Pd- and Ag-Loaded Membranes Obtained by Means of XRD, TEM, and XAFS[a]

film		in	XRD L/Å	TEM D/Å	XAFS, Pd-edge				
					D/Å	l_{ox}/Å	n(Pd−O)	n(Pd−Pd)	T/K
1	Pd	air	12, *40(30)*	10−30, *200**	24(10)	4.0(9)	2.5	2.8	80
2	Pd	air	9, *44(20)*	10, *140**	14(4)	3.0(9)	2.8	1.3	300
2	Pd	H_2			13(2)	1.5(3)	(1.4)	3.7	300
3	Pd	air	10, *70(10)*	10, *200#*	13	2.4	2.5	1.6	80
3	Pd	air	10, *70(10)*	10, *200#*	12	2.2	2.5	1.4	300
4	Pd	air	13, 50(30)	10−30, *200**	17	2.6	(2.0)	3.3	80
5	Pd	air		50−100[f]	39	3.0	(1.1)	7.1	300
6	Pd	air	23(7)	10−30[f]	52	4.2	(1.2)	7.2	80
bulk	Pd	air			>1000		(0.0)	12.0	300
bulk	Pd	H_2			>1000		(0.2)	11.2	300
7	Pd	air	*30*, 80(40)		50−220	(5)	(1.0)	8.1	300
7	Pd	H_2			40−120	(1.9)	(0.4)	9.6	300
8	Ag	air	70(20)	35−140					300
9	Ag	air	70(20)	15−35					300

[a] L denotes the grain size of the cluster metal core; D, the cluster diameter. In most films, XRD and TEM show a bimodal size distribution. Two characteristic sizes are given in these cases, where numbers in italics indicate minority components (supercripts: * a few dense particles, # scattered particles, [f] agglomerates). XAFS measures an intermediate size over the whole cluster ensemble. From the given mean XAFS coordination numbers n, mean cluster diameters D and mean oxide layer thicknesses l_{ox} are calculated assuming the onion model (see the Appendix). For the XAFS coordination numbers given in parentheses, the MSRD has not been varied in the two-shell fit.
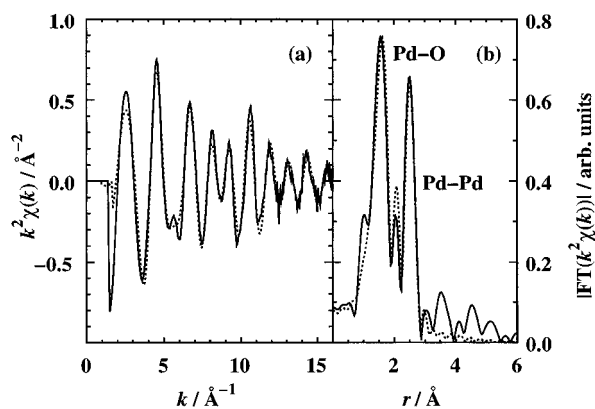

Figure 8. (a) Pd XAFS spectrum $k^2\chi(k)$ and (b) corresponding Fourier transform (FT) magnitude $|FT(k^2\chi(k))|$ of Pd-loaded membrane 3, measured at 80 K. The first and second peak correspond to Pd−O and Pd−Pd nearest neighbor distances in the sample, i.e. oxidized and metallic Pd. The dotted lines are the two-shell fit results.

different metal precursors. Cluster size distributions are investigated in more detail in the next section (see Table 7).

For catalytic properties it is essential whether the two (or more) metal species are present in the membrane in their respective elemental or in alloyed form. In this respect, because of being element specific, XAFS is a suitable tool. Table 6 summarizes the results from XAFS measurements at both metal species (Pd and X = Ag, Pb, Cu, or Co) and XRD experiments.

Figure 11 shows XRD scans of Pd/Ag-loaded membranes 11 and 12 and Pd/Cu-loaded membrane 16. Reflection peaks are weak and broadened, indicating nanosized particles in the membranes. Only in membrane 12 are sharp Bragg peaks observed, which can be assigned to metallic Ag. Likely, the scattered large particles seen in TEM are these Ag particles. The broad peak around $2\Theta = 40°$ in membrane 12 is clearly shifted with respect to the Ag(111) peak and is due to nanosized Pd particles. From Figure 11b it is therefore concluded that in the larger particles which can be detected by XRD no alloying of Pd and Ag occurs. In membrane 11, no large Ag clusters are seen (Figure 11a). The broad diffraction peak around $2\Theta = 40°$ may result from a superposition of small metallic Ag and Pd particles, as might be indicated by the small hump on the low-Θ side, but the present data quality does not allow us to address the question of metal alloying unambiguously. These
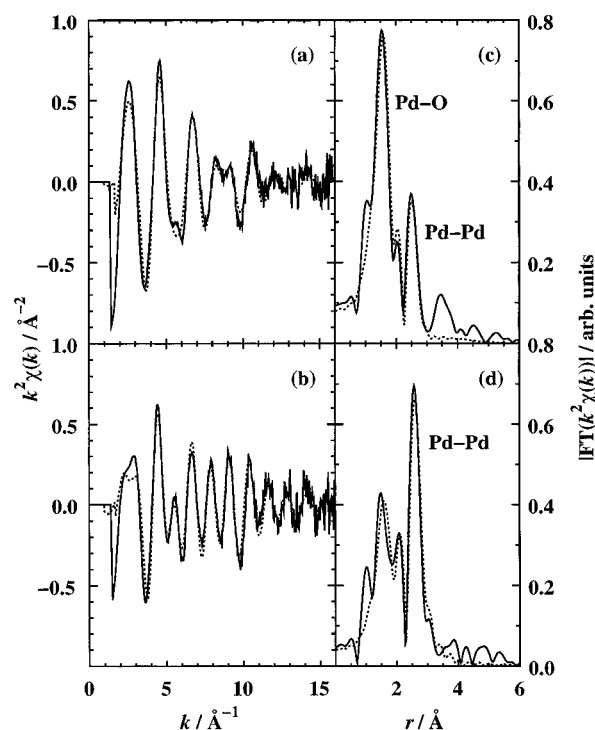

Figure 9. Pd XAFS spectra $k^2\chi(k)$ of Pd-loaded membrane 2 at 300 K (a) before and (b) after reduction with H_2, performed at 300 K for 45 min. Solid lines represent the raw experimental data after background correction; dotted lines, the fit results from two-shell fits (see the Experimental Section). Corresponding XAFS Fourier transform magnitudes $|FT(k^2\chi(k))|$ (c) before and (d) after reduction with H_2. Due to the reduction, the second peak (Pd−Pd contribution) increases, whereas the first peak (Pd−O contribution) decreases. Note that, compared to Figure 8b, the second Pd−Pd peak in the FT of part c is smaller, although the mean cluster size is about the same because the MSRD is larger at room temperature.

XRD data are also consistent with the TEM of Figure 10a in the sense that they support an aggregation of smaller particles to larger ones without formation of larger crystalline grains, which would lead to sharper diffraction peaks. The XRD spectrum of membrane 16, 1:1 Pd/Cu, does not show any structure besides the very weak reflection around $2\Theta = 42°$ (Figure 11c). As for the monometallically loaded membranes, particle sizes were estimated from the XRD data whenever possible (see Table 7). In all membranes except for 14−16,
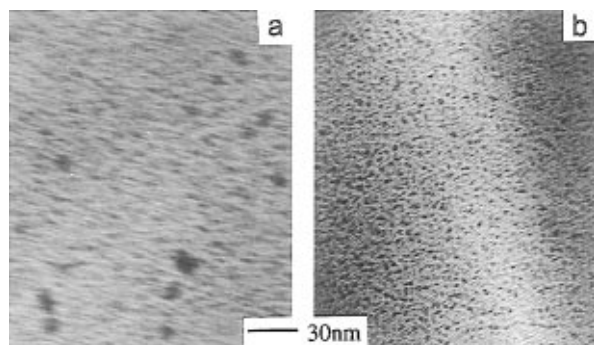
Figure 10. TEM picture of Pd/Ag-loaded membranes prepared in NMP: (a) membrane 11, prepared from metal precursor AgBF₄; (b) membrane 12, prepared from metal precursor AgAc.

Figure 11. XRD scans of (a) Pd/Ag-loaded membrane 11, (b) Pd/Ag-loaded membrane 12, and (c) Pd/Cu-loaded membrane 16. Each of the vertically shifted spectra takes up a third of the entire intensity scale.

reflections are clearly lying at angular positions of corresponding fcc metals in their elementary form. In the last column of Table 6, the downscaled lattice constant $a/\sqrt{2}$ is listed, which is identical to the nearest neighbor distance for fcc lattices. It should be noted that entries in normal typeface indicate fcc lattice formation because they result from more than one fitted XRD peak, whereas entries in italics are rescaled lattice spacings, only.

Metal–metal interaction can most effectively be investigated from the minority atom species. In the first three columns, Table 6 contains the results of XAFS measurements at the K-edge of atoms X. As shown for membranes 12 and 16 in Figure 12, the XAFS FTs which reflect the coordination shells around the atoms X are dominated by one peak each. Ag in membranes 11 and 12 is present in nonoxidized form (e.g. Figure 12a,b). Interatomic distances obtained from single-shell XAFS fits are $R(\text{Ag–Ag}) = 2.82(2)$ Å and 2.87(2) Å, respectively, with a mean coordination number of $n(\text{Ag–Ag})$ around 9. To the contrary, in membranes 13–20, the atoms X = Pb, Cu, Co are coordinated by oxygen (Figure 12c,d). Table 6 shows mean coordination numbers $n(\text{X–O})$ and interatomic distances $R(\text{X–O})$ obtained from one-shell XAFS fits. In Pd/Cu membranes Cu is tetrahedrally coordinated by oxygen; in Pd/Co, octahedrally, similar to the bulk oxides CuO and CoO, respectively. Also, measured bond lengths are consistent with the oxide values. From the absence of higher shells it is concluded that Cu and Co furthermore are incorporated in the membranes in high dispersion and/or with high disorder. No indication of Cu and Co metal formation is found. Due to its low debye temperature, Pb is hard to measure in XAFS. The accuracy of the Pb results is therefore poor, and higher shells might be highly
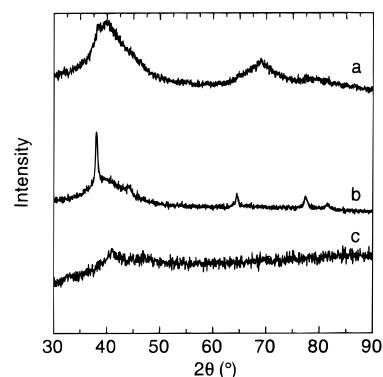
suppressed in the FT. However, also Pb is, at least partly, present in nonmetallic form.

XAFS spectra at the Pd K-edge of membranes 11–14 are very similar to the ones in Pd monometallically loaded films and were fitted well in a similar way by Pd–O and Pd–Pd contributions. From the fit results, only the distances $R(\text{Pd–Pd})$ are given in Table 6. The question of metal–metal interaction is discussed further below for these membranes. As shown in Figure 13, in the 1:1 bimetallic Pd/Cu membrane 16 the Pd XAFS is significantly changed. In the distance range $r = 1.3–3.0$ Å of the FT of Figure 13b, three peaks are seen. In addition to Pd–O and Pd–Pd shells, which still are present, a strong third contribution at about $r = 1.9$ Å appears. By means of three-shell fits we elucidated other possible atoms being bound to Pd in the membrane. Numerous fits showed that the additional contribution is not due to Pd–Cu bonds. This is well supported by the fact that Cu is fully oxidized in the membrane, as discussed above, with no higher shells visible in the Cu XAFS Fourier transform. Instead, the experiment is modeled very well by a three-shell fit (dotted lines in Figure 13) assuming a Pd–Cl coordination in the membrane. Obviously, Cl from the CuCl₂ precursor partly reacts with Pd in the course of nanoparticle formation. Formation of Pd/Cl species was also observed recently by Gloor et al.[49] Figure 14 shows a comparison of Pd XAFS FTs for the Pd monometallically loaded membrane 3 (dotted line), the 9:1 Pd/Cu-loaded membrane 18 (thin solid line), and the 1:1 Pd/Cu-loaded membrane 16 (thick solid line). As is also obtained from quantitative fitting, an increase of the Pd–Cl contribution is observed in Figure 14 with increasing

TABLE 6: Coordination Numbers *n*, Interatomic Distances *R*, and Lattice Constants *a* from XAFS and XRD Analyses of Bimetallically Loaded Membranes Pd/X*[a]**

	film Pd/X	XAFS at atom X			XAFS at Pd $R(\text{Pd–Pd})$ (Å)	XRD $a/\sqrt{2}$ (Å)
		$n(\text{X–O})$	$n(\text{X–X})$	$R(\text{X–O})$ (Å)		
11	Pd/Ag(3:1)		8.8(9)	2.82(2)*	2.75(2)	2.75–2.90
12	Pd/Ag(3:1)		8.6(9)	2.87(2)*	2.76(2)	2.75(2), 2.89(1)
13	Pd/Pb(1:1)	2.0(9)		2.27(9)	2.75(2)	amorphous
14	Pd/Pb(9:1)	1.5(9)	yes	2.25(9)	2.78(2)	2.81(2)
15	Pd/Cu(1:1)	3.9(9)		1.94(3)	2.72(4)	*2.65(2)*
16	Pd/Cu(1:1)	4.1(5)		1.97(2)	2.73(4)	*2.67(2)*
17	Pd/Cu(3:1)	4.2(5)		1.96(2)	2.71(4)	amorphous
18	Pd/Cu(9:1)	3.6(9)		1.95(3)	2.76(3)	2.77(1)
19	Pd/Cu(9:1)		not measured		2.73(3)	2.75(2)
20	Pd/Co(9:1)	6.7(9)		2.04(6)	2.75(2)	2.75(1)

[a] * denotes distances $R(\text{Ag–Ag})$. For comparison, interatomic distances are 2.75 Å in Pd metal, 2.89 Å in Ag metal, 3.50 Å in Pb metal, 2.56 Å in Cu metal, and 2.51 Å in Co metal.[48] Entries in regular typeface of reduced XRD lattice constant $a/\sqrt{2}$ indicate the formation of a fcc lattice. See text for discussion. Temperatures for the Pd XAFS measurements were 80 K except for samples 11, 13, and 15, which were measured at 300 K. Temperatures for XAFS measurements at the atoms X were 300 K for samples 11, 13, and 15; 80 K for 12, 14, 18, and 20, and 20 K for 16 and 17.

Metal Nanoclusters in PAI Films

J. Phys. Chem. B, Vol. 101, No. 8, 1997 **1287**

TABLE 7: Mean Cluster Sizes in Bimetallically Loaded Membranes Obtained by Means of XRD, TEM, and XAFS[a]

	film Pd/X	in	XRD L/Å	TEM D/Å	XAFS at Pd		XAFS at X
					D/Å	l_{ox}/Å	D'/Å
11	Pd/Ag(3:1)	air	15	20, *80**	17(4)	3.1(9)	17
11	Pd/Ag(3:1)	H$_2$			15(2)	1.5(2)	
12	Pd/Ag(3:1)	air	Pd, 11; Ag, 150(80)	8–20, *400#*	12	2.2	16
13	Pd/Pb(1:1)	air	amorphous		12.3	2.8	non met.
13	Pd/Pb(1:1)	H$_2$			13.1	1.7	
14	Pd/Pb(9:1)	air	7, *40(20)*		12.3	2.3	?
15	Pd/Cu(1:1)	air	20(10)		?	?	non met.
16	Pd/Cu(1:1)	air	20		?	?	non met.
17	Pd/Cu(3:1)	air	8		?	?	non met.
18	Pd/Cu(9:1)	air	10, *60(30)*		~15	~2	non met.
19	Pd/Cu(9:1)	air	8, *90(40)*		~15	~2	non met.
20	Pd/Co(9:1)	air	7, *40(10)*		~15	~2	non met.

[a] L denotes the grain size of the cluster metal core; D, the cluster diameter. As in Pd- and Ag-loaded films, a bimodal size distribution is observed in most samples (see caption of Table 5). The environment at the atoms X in the membranes in many cases is observed to consist of nonmetallic atoms (e.g. oxygen).
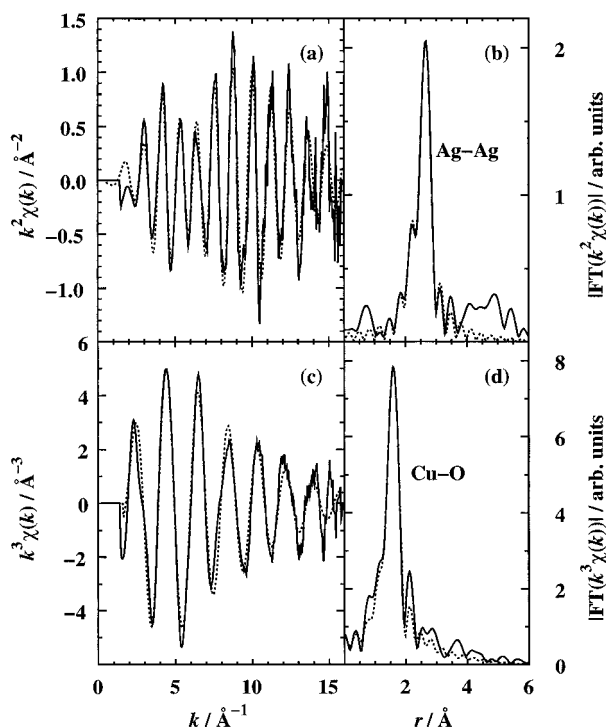

Figure 12. (a) Ag XAFS spectrum $k^2\chi(k)$ and (b) corresponding Fourier transform magnitude $|FT(k^2\chi(k))|$ of Pd/Ag-loaded membrane 12, measured at 80 K. The spectra show metallic Ag clusters. The dotted lines are Ag–Ag single-shell fit results. (c) Cu XAFS spectrum $k^3\chi(k)$ and (d) corresponding Fourier transform magnitude $|FT(k^3\chi(k))|$ of Pd/Cu-loaded membrane 16, measured at 20 K. The spectra show oxidized Cu. The dotted lines are Cu–O single-shell fit results.

Figure 13. (a) Pd XAFS spectrum $k^2\chi(k)$ and (b) corresponding Fourier transform magnitude $|FT(k^2\chi(k))|$ of Pd/Cu-loaded membrane 16, measured at 80 K. As discussed in the text, the presence of Pd–Cl in addition to Pd–O and Pd–Pd contributions is observed.

Figure 14. Comparison of Pd XAFS Fourier transforms for the Pd monometallically loaded membrane 3 (dotted line), the 9:1 Pd/Cu-loaded membrane 18 (thin solid line), and the 1:1 Pd/Cu-loaded membrane 16 (thick solid line). As the Cu content increases, an increasing Pd–Cl contribution occurs.

amount of Cu originating from the CuCl$_2$ precursor during membrane preparation. Three-shell fits performed on the Pd XAFS data of membranes 15–20 in all cases give an interatomic distance R(Pd–Cl) = 2.30–2.34 Å compared to an interatomic distance Pd–Cl in PdCl$_2$ of 2.31 Å.[48] Formation of Pd–Cl bonds is also consistent with X-ray absorption near edge spectroscopy (XANES). A ~1 eV shift of the Pd K-edge toward higher energies occurs for membranes 15 and 16 with respect to Pd monometallically loaded membranes.

From the results of Table 6, interactions between the two metal species in the membranes are recognized as follows. In Pd/Ag membrane 11, Pd XAFS gives exactly the interatomic distance in Pd metal (2.75 Å), whereas Ag XAFS gives a smaller value than in Ag metal (2.89 Å). Ag and Pd cannot be distinguished by XAFS as backscattering atoms since they are lying next to each other in the periodic table. Therefore, in a
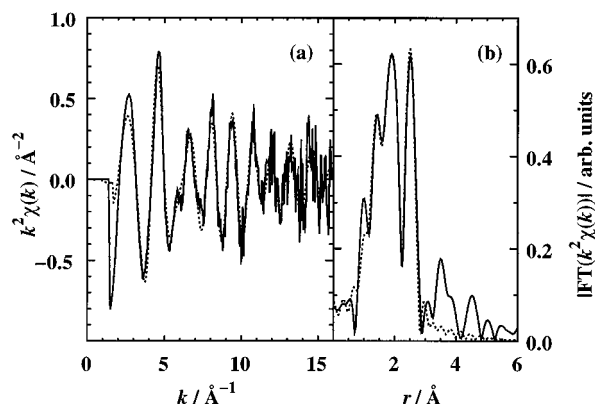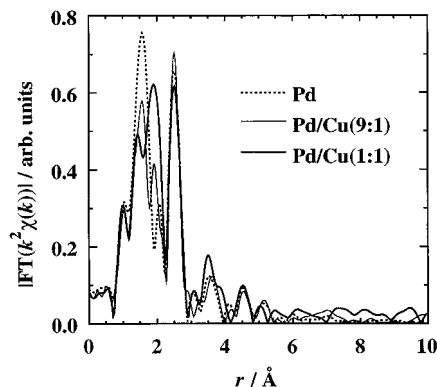
homogeneous solid solution, average values would be obtained from the XAFS fits, namely, 2.80 Å for both Pd and Ag, according to Vegard's law. This is not observed in the experiment. The lowering of R(Ag–Ag), however, can be explained by a partial alloying of Ag and Pd in the film. This is in accordance with the XRD spectrum. To the contrary, in Pd/Ag membrane 12, metallic Ag and Pd distances are clearly measured both by XAFS and XRD and alloying is unlikely. Also, in Pd/Pb(1:1)-loaded membrane 13, metal–metal interaction is not seen since no additional contribution R(Pd–Pb) around 3.13 Å is observed. Consistent small distance shifts

TABLE 8: Pd Cluster Lattice Expansion Due to Hydrogen Interdiffusion for a Number of Membranes in Comparison to Pd Bulk Measured by Means of XAFS[a]

	film	ΔR(Pd−Pd)/Å	R_{air}(Pd−Pd)/Å	D/Å
2	Pd	0.057	2.747	14
7	Pd	0.073	2.755	∼100
	Pd bulk	0.020	2.751	>1000
11	Pd/Ag(3:1)	0.046	2.753	17
13	Pd/Pb(1:1)	0.065	2.754	12
15	Pd/Cu(1:1)	(0.022)	(2.719)	

[a] The expansion is independent of mean cluster sizes in the membranes but considerably larger than in the bulk. The error of ΔR(Pd−Pd) is ±0.01 Å, except for the film Pd/Cu, where due to the uncertainties of the three-shell fit, it is ±0.04 Å.

seen in XAFS and XRD in Pd/Pb(9:1) membrane 14 indicate the formation of some bimetallic clusters, supported by the presence of a small, second peak in the Pb XAFS FT. Note the different Pd/Pb ratio in the two membranes. Under different preparation conditions core−shell structures of bimetallic noble metal clusters Pd/Pt, Pd/Au, Au/Pt, and Pd/Rh are achieved.[1,16,50,51]

In Pd/Cu- and Pd/Co-loaded membranes 15−20, XAFS shows the formation of oxidized, highly dispersed and/or highly disordered Cu or Co, the presence of metallic Pd particles, and the formation of Pd−Cl bonds. The more chlorine present in the polymer/metal salt precursor solution, the larger the Pd−Cl contribution. The observed small distance reduction of R(Pd−Pd) is within experimental error. The shift of the broad XRD reflection in membranes 14−16 is most likely due to the presence of other phases (Pd−Pb, Pd−Cl, Cu−O) than the elementary metallic ones.

Cluster Size Distributions in Bimetallically Loaded Membranes. Table 7 lists average cluster sizes determined in bimetallically loaded membranes 11−20. The majority of metallic clusters have diameters between 10 and 30 Å. Results from the different methods are again well consistent. In addition, as in the Pd-loaded membranes, a minority of larger clusters or aggregates is often incorporated in the membranes. Pd particle sizes were calculated from Pd XAFS coordination numbers when two-shell fits decribed well the experimental data. In Pd/Cu and Pd/Co membranes, due to the Pd−Cl contribution discussed in the previous section, Pd particle sizes cannot be estimated. A more complicated model than the onion model would have to be applied. Ag particle sizes were calculated from Ag XAFS data from the reduction of the mean coordination number (see the Appendix).

It is noticeable that Ag particle sizes calculated from Ag XAFS in the Pd/Ag membranes are significantly lower than the values obtained by XRD. A possible explanation is that about 25% of Ag in the membranes is not incorporated in metallic clusters and is highly disordered. This would reduce the mean XAFS coordination number (and thereby the obtained mean particle size) but would not contribute to the XRD signal. Cluster sizes in Pd/Pb membranes are among the smallest obtained in bimetallic membranes.

Reduction behavior of the Pd clusters is observed to be similar as that in purely Pd-loaded membranes. In Pd/Ag as well as in Pd/Pb membranes, room temperature H_2 reduction reduces the oxide layer thickness by a factor of about 2.

Lattice Expansion Due to Hydrogen Interdiffusion. Table 8 shows the effect of room temperature H_2 reduction for 45 min on the nearest neighbor distance R(Pd−Pd) in membranes in comparison to Pd bulk as measured by Pd XAFS. In the membranes, a linear lattice expansion of about 2.2% is observed, which, within experimental error, is independent of the average particle size in the sample. In Pd bulk, the expansion is below

1%. The result for the Pd/Cu membrane 15 is extracted from three-shell fits and exhibits a much larger error. In addition to reducing the oxide surface layer of the Pd particles, hydrogen diffuses into the Pd metal phase, thereby expanding the lattice. At room temperature, two phases of palladium hydride coexist: the low hydrogen content α phase (maximum atomic fraction $c = \alpha_{MAX} = 0.008$ of hydrogen atoms per palladium atom) and the highly distorted, largely expanded, hydrogen-rich β phase (minimum atomic fraction $c = \beta_{MIN} = 0.607$).[52] At intermediate hydrogen concentrations of $\alpha_{MAX} \leq c \leq \beta_{MIN}$ the measured macroscopic lattice expansion originates from the formation of the β phase at the expense of the α phase. From the known volume expansion of 19% due to solution of one hydrogen atom per palladium atom in this transition region,[53] we calculate an atomic fraction of hydrogen atoms $c = 0.35(6)$ in the room temperature reduced membranes summarized in Table 8. Note that the reduction time of 45 min is within the order of the measured time lag for a single membrane. Stacks of about six films were used for the XAFS reduction experiments.

Conclusion

Combining different structural techniques, nanocrystalline metallic clusters in both monometallically loaded (Pd, Ag) and bimetallically loaded PAI membranes (Pd/Ag, Pd/Cu, Pd/Co, Pd/Pb) were detected and characterized. Structure and cluster size distributions in the membranes were investigated in detail. In this respect, each of the structural techniques employed has its particular strengths and weaknesses so that only the combination yields an accurate full picture. TEM gives real space images with a very large amount of local information, but due to the small investigated sample volume observations cannot be transferred without uncertainties to the entire membrane volume. Also, small cluster <1 nm cannot easily be resolved by TEM techniques. XRD allows an accurate characterization of crystalline particles above a critical size and probes the volume of the membranes, but is also not sensitive to small clusters. Small clusters around 1 nm can be well characterized by the local probe of XAFS. Furthermore, XAFS is element specific, which allows the investigation of reactions on a length scale invisible to XRD, as shown for the Pd/Cu membranes. However, XAFS always measures an average over all atomic environments of the selected atoms and cannot distinguish, as TEM and XRD, between small and large particles, which are both present in the membranes. Information on an average size of the nanoparticles, however, is obtained from XAFS coordination numbers. The onion model presented allows the determination of effective metal core and oxide layer dimensions of oxidized nanoparticles. In view of the above sensitivities of each employed technique the structural results given in Tables 5−7 are in very good agreement.

The bimodal size distribution observed in most of the films is most likely connected to the high metal loading of 15 wt %. At these high loadings, high concentrations of small clusters are generated in the membrane; that is, clusters are located close to each other and have to diffuse only short distances through the membrane to form some larger particles or aggregates. It should be noted, however, that XRD and XAFS show that the great *majority* of clusters have sizes typically <3 nm in PAI membranes, which is anticipated for efficient catalytic properties. The structure of the metal clusters in the membranes is found to be stable over periods of at least one year under atmospheric conditions, as was shown by repeating experiments.

Cluster size distributions are clearly different when using silicone instead of PAI as a cluster protectant. In silicone, bigger aggregates up to 80 nm represent a considerable fraction or even

Metal Nanoclusters in PAI Films

J. Phys. Chem. B, Vol. 101, No. 8, 1997 **1289**

the majority in the membrane. Most likely, higher diffusivities in silicone allow atoms to more easily form larger aggregates. Membranes optimized for catalytic applications exhibit high gas permeabilities for gases of the catalytic reaction but also a large inner surface of the catalytically active region of the membrane, i.e. low tendencies for cluster aggregation. It will be a future goal to optimize these two competing properties within the same membrane by adjusting the protective role of the polymer together with the reduction process.

The solvent used in the preparation of the metal-loaded membranes has a strong influence on the resulting metal cluster sizes. NMP, the better solvent for the polymer, is more favorable than THF. Independently, the stirring time of the polymer/metal precursor solution is observed to be a sensitive parameter of the resulting size distribution. Only complete solution of the polymer chains on a molecular level can allow an optimum distribution of the metal precursor salt within the polymer chains. At stirring times of at least 3 hours, this appears to be fulfilled, which, upon reduction, results in nanosized, homogeneously distributed metal clusters. The metal salt precursor used in the preparation also controls resulting cluster sizes, as indicated in the Ag-loaded membranes. This will have to be studied in more detail in the future.

In most bimetallic films, no or weak indications of formation of *bimetallic clusters* are found. This even holds for the Pd–Ag system, forming a fcc solid solution over the entire concentration range.[54] It is remarkable also in the Pd–Cu, Pd–Co, and Pd–Pb systems because they do not show miscibility gaps between the terminal solid solutions but rather ordered intermetallic phases.[54] At room temperature, low mobilities may hinder the ordering process, so that fcc solid solutions would be expected in these systems from a pure metallurgical point of view. However, the type of metal precursors used, the reduction process applied, and the kinetics during cluster formation inside the polymer are believed to induce the formation of elementary metallic clusters. The redox potentials of the metal ions used in the present study are considerably lower than the ones used in ref 16, where, under different conditions, core–shell structures of bimetallic clusters were stabilized.

Transition metal chloride precursors, as were used in Pd/Cu and Pd/Co membranes, are observed to react with Pd from the palladium acetate precursor in the course of the reduction step during membrane preparation under formation of Pd–Cl bonds. A similar interaction was not observed in ref 16, where polymer-protected bimetallic noble metal clusters could be prepared in PVP from noble metal chloride precursors of all constituents.

Consistent with their small size, Pd clusters in PAI membranes are reversibly oxidized/reduced by air/hydrogen already at room temperature, as shown by gas permeation in the membrane mode and XAFS. In addition to oxide reduction, hydrogen diffuses into the Pd crystal lattice of the nanoclusters, thereby expanding it. From the measured Pd–Pd bond length expansion a storage of one hydrogen atom per three Pd atoms is achieved at ambient conditions.

Appendix

In this Appendix, the details of the onion model are presented, which is used to determine the size and oxide layer thickness of oxidized metal clusters from measured XAFS coordination numbers.

At a cluster surface, the coordination of atoms is smaller than in the bulk. Therefore, mean coordination numbers measured by XAFS decrease with increasing surface-to-volume ratio and decreasing size of a cluster. This has been used in the past to determine metal particle sizes from XAFS coordination numbers by use of simple geometrical models for the particle shape[55–60] and recently also by use of molecular dynamics simulation.[43] The applied models in these references can be used to determine the metal core size of oxidized particles as well, but, as an oxide surface layer may contribute significantly to the volume of nanoparticles, an extended onion model is presented.

Figure 15 shows a schematic view of an idealized, oxidized, spherical Pd cluster. The inner metal core of diameter d is surrounded by an oxide layer of thickness l_{ox}. In the interface region marked by the dashed circles, Pd atoms in the core and Pd atoms in the oxide layer have reduced nearest neighbors coordination. As is also commented on in the Experimental Section, the measured XAFS coordination numbers $n(\text{Pd–O})$ and $n(\text{Pd–Pd})$ are given by

$$n(\text{Pd–O}) = 4f_O^{\text{ring}}(d,l_{ox})[1 - p(d,l_{ox})] \tag{2}$$

$$n(\text{Pd–Pd}) = 12f_{\text{Pd}}(d)\,p(d,l_{ox}) \tag{3}$$

where $p(d,l_{ox})$ is the percentage of Pd atoms in the metallic core of the cluster with respect to the total amount of Pd. $f_O^{\text{ring}}(d,l_{ox})$ and $f_{\text{Pd}}(d)$ are the normalized mean coordination numbers of Pd–O and Pd–Pd bonds due to surface effects in the oxide layer ring and in the metal core, respectively. The functions f vary between zero in a single-atom cluster and approach unity in the bulk. For spherical particles, the percentage p is linked to the volume percentage q of the Pd metallic core by

$$p(d,l_{ox}) = \cfrac{1}{1 + \cfrac{M_{\text{Pd}}\rho_{\text{PdO}}[1 - q(d,l_{ox})]}{M_{\text{PdO}}\rho_{\text{Pd}}q(d,l_{ox})}} \tag{4}$$

where

$$q(d,l_{ox}) = \frac{(d/2)^3}{(d/2 + l_{ox})^3} \tag{5}$$

M and ρ denote the molecular weight and mass density.
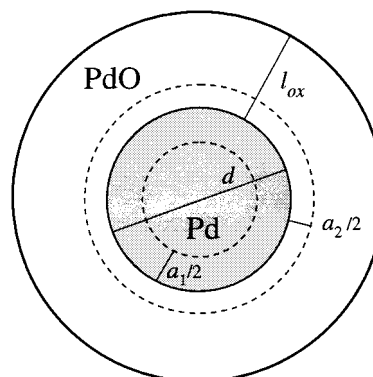

Figure 15. Schematic picture of an oxidized Pd metal particle consisting of a metallic inner core with diameter d and an oxidized surface layer of thickness l_{ox}. The interface region is marked by the dashed circles.

Recently, exact analytical formulas for mean XAFS coordination numbers in clusters have been reported for different cluster geometries such as tetrahedron, octahedron, and icosahedron as a function of total atoms N_{tot} in the cluster.[61,62] They can be formulated in terms of an effective cluster diameter d of a sphere containing the identical number of atoms by applying

$$d = (3\sqrt{2}/\pi)^{1/3}aN_{tot}^{1/3} \qquad (6)$$

where a is the nearest neighbor distance. This equation is exact for an fcc closed package structure. For metallic Pd clusters with $a_1 = 2.75$ Å the exact normalized mean coordination number $f_{Pd}(d)$ from ref 62 can be well approximated for cluster sizes between 7 and 80 Å by the simple form

$$f_{Pd}(d) = 1 - 4.5 \text{ Å}/d \qquad (7)$$

This approximation more closely follows tetrahedral than other cluster geometries since it is assumed that the actual clusters will have imperfect surfaces resulting in an enlarged surface area in comparison to ideal cluster geometries, such as icosahedra or cuboctahedra.

The normalized mean coordination number in the oxide surface layer $f_O^{ring}(d,l_{ox})$ is determined in the following. Since no exact direct formulas are available from the literature in this case, the results of ref 62 are transferred to this situation by applying a continuum description.

First, the outer surface of the oxide layer is assumed to be fully terminated by oxygen and, consequently, not to contribute to the coordination number reduction. To determine the effect of the Pd−PdO interface, we first consider an isolated, spherical PdO particle of diameter d identical to the Pd core, which is not terminated by oxygen at its outer surface. In analogy to the approximation described above for the Pd core, the normalized mean coordination number $f_0(d)$ in this PdO particle is well described by

$$f_0(d) = 1 - 3.2 \text{ Å}/d \qquad (8)$$

For a given cluster size the coordination number reduction is smaller in PdO due to the reduced nearest neighbor distance of $a_2 = 2.02$ Å in comparison to Pd metal. On the basis of this expression, a mean normalized coordination $x(d)$ of Pd−O in the surface layer of thickness $a_2/2$ of the hypothetical PdO particle can then be defined by

$$f_0(d) = q_{inner}(d,a_2) + q_{surf1}(d,a_2)\, x(d) \qquad (9)$$

where $q_{inner}(d,a_2) = (d/2 - a_2/2)^3(d/2)^{-3}$ and $q_{surf1}(d,a_2) = 1 - q_{inner}$ are the volume fractions of interior and surface of the PdO particle. (The chosen surface layer thickness yields $x(D) = 0.5$ in the bulk limit.) The mean normalized coordination $x^{ring}(d)$ of Pd−O *in the interfacial layer of the oxidized part of the Pd particle*, limited by the outer dashed line in Figure 15, is given as the complement of $x(d)$:

$$x^{ring}(d) = 1 - x(d) \qquad (10)$$

Therefore, the normalized mean coordination number in the oxide surface layer $f_O^{ring}(d,l_{ox})$ is yielded by

$$f_O^{ring}(d,l_{ox}) = q_{outer}(d,a_2,l_{ox}) + q_{surf2}(d,a_2,l_{ox})[1 - x(d)] \qquad (11)$$

where

$$q_{outer}(d,a_2,l_{ox}) = [(d/2 + l_{ox})^3 - (d/2 + a_2/2)^3]/[(d/2 + l_{ox})^3 - (d/2)^3] \qquad (12)$$

and

$$q_{surf2}(d,a_2,l_{ox}) = 1 - q_{outer} \qquad (13)$$

are the outer and interface volume fractions of the surface oxide, respectively. After substituting eqs 4, 5, 7−9, and 11−13 into eqs 2 and 3, from the experimentally measured XAFS coordination numbers $n(Pd-O)$ and $n(Pd-Pd)$ the oxide surface layer thickness l_{ox} and the total diameter $D = d + 2l_{ox}$ of the Pd particle are obtained.

As applied to Ag-loaded membranes, sizes of nonoxidized particles are calculated by means of simplified eq 3,

$$n(Ag-Ag) = 12f_{Ag}(d) \qquad (14)$$

where $f_{Ag}(d) \approx f_{Pd}(d)$ in good approximation.

References and Notes

(1) *Clusters and Colloids*; Schmid, G., Ed.; VCH: Weinheim, 1994.
(2) Henglein, A. *J. Phys. Chem.* **1993**, *97*, 5457.
(3) Pomogailo, A. D. *Platinum Met. Rev.* **1994**, *38*, 60.
(4) Gleiter, H. *Prog. Mater. Sci.* **1989**, *33*, 223.
(5) Siegel, R. W.; Fougere, G. E. In *Nanophase Materials: Synthesis−Properties−Applications*; Hadjipanayis, G. C., Siegel, R. W., Eds.; Kluwer: Dordrecht, 1994; p 233ff.
(6) Trudeau, M. L.; Ying, J. Y. *Nanostruct. Mater.* **1996**, *1/2*, 245.
(7) Hirai, H.; Chawanya, H.; Toshima, N. *React. Polym.* **1985**, *3*, 127.
(8) Toshima, N. *J. Macromol. Sci.-Chem.* **1990**, *A27*, 1225.
(9) Bradley, J. S.; Millar, J. M.; Hill, E. W. *J. Am. Chem. Soc.* **1991**, *113*, 4016.
(10) Kiwi, J.; Grätzel, M. *J. Am. Chem. Soc.* **1979**, *101*, 7214.
(11) Bönnemann, H.; Brijoux, W.; Brinkmann, R.; Dinjus, E.; Jonssen, T.; Korall, B. *Angew. Chem.* **1991**, *103*, 1344; *Angew. Chem., Int. Ed. Engl.* **1991**, *30*, 1312.
(12) Toshima, N.; Takashi, T. *Bull. Chem. Soc. Jpn.* **1992**, *65*, 400.
(13) Turkevich, J.; Kim, G. *Science* **1970**, *169*, 873.
(14) Behr, A.; Schmidke, H. *Chem.-Ing.-Tech.* **1993**, *65*, 568.
(15) Bradley, J. S.; Hill, E. W.; Behal, S.; Klein, C. *Chem. Mater.* **1992**, *4*, 1234.
(16) Yonezawa, T.; Toshima, N. *J. Chem. Soc., Faraday Trans.* **1995**, *91*, 4111, and references therein.
(17) Toshima, N.; Harada, M.; Yonezawa, T.; Kushihashi, K.; Asakura, K. *J. Phys. Chem.* **1991**, *95*, 7448.
(18) Ng Cheong Chan, Y.; Craig, G. S.; Schrock, R. R.; Cohen, R. E. *Chem. Mater.* **1992**, *4*, 885.
(19) Fritsch, D.; Peinemann, K.-V. *Proceedings of the 3rd European Technical Symposium on Polyimides and High Performance Polymers (STEPI 3)*, Le Corum, Montpellier, June 1−3, 1993; J. M. Abadie: Montpellier, France, 1993.
(20) Fritsch, D.; Peinemann, K.-V. *J. Membr. Sci.* **1995**, *99*, 29.
(21) Fritsch, D.; Peinemann, K.-V. *Catal. Today* **1995**, *25*, 277.
(22) Gao, H.; Xu, Y.; Liao, S.; Liu, R.; Yu, D. *J. Appl. Polym. Sci.* **1993**, *50*, 1035.
(23) Shim, I. W.; Kim, K. S.; Kim, S. K.; Oh, W. S.; Oh, S. J.; Yang, Y. S.; Suh, H. K.; Lee, S. *React. Polym.* **1994**, *23*, 187.
(24) Gao, H.; Xu, Y.; Liao, S.; Liu, R.; Liu, J.; Li, D.; Yu, D.; Zhao, Y.; Fan, Y. *J. Membr. Sci.* **1995**, *106*, 213.
(25) Waller, F. J. *Catal. Rev.-Sci. Eng.* **1986**, *28*, 1.
(26) Hodges, A. M.; Linton, M.; Mau, A. W.-H.; Cavell, K. J.; Hey, J. A.; Seen, A. J. *Appl. Organomet. Chem.* **1990**, *4*, 465.
(27) Pehnt, M.; Schulz, D. L.; Curtis, C. J.; Jones, K. M.; Ginley, D. S. *Appl. Phys. Lett.* **1995**, *67*, 2176.
(28) Davis, S. C.; Klabunde, K. J. *Chem. Rev.* **1982**, *82*, 153.
(29) Vasil'kov, A. Y.; Olenin, A. Y.; Sergeev, V. A.; Karanov, A. N.; Olenina, E. G.; Gryaznov, V. M. *J. Cluster Sci.* **1991**, *2*, 117.
(30) Sergeev, G.; Zagorsky, V.; Petrukhina, M. *J. Mater. Chem.* **1995**, *5*, 31.
(31) El-Shall, M. S.; Slack, W. *Macromolecules* **1995**, *28*, 8456.
(32) Watkins, J. J.; McCarthy, T. J. *Chem. Mater.* **1995**, *7*, 1991.
(33) Reetz, M. T.; Helbig, W. *J. Am. Chem. Soc.* **1994**, *116*, 4701.
(34) Fritsch, D.; Avella, N. *Macromol. Chem. Phys.* **1996**, *197*, 701.
(35) Henis, J. M. S.; Tripodi, M. K. *J. Membr. Sci.* **1981**, *8*, 233.
(36) Williamson, G. K.; Hall, W. H. *Acta Metall.* **1953**, *1*, 22.
(37) Scherrer, P. *Nachr. Göttinger Gesellsch.* **1918**, 98.

(38) Warren, B. E. *X-Ray Diffraction*; Dover Publications: New York, 1990.

(39) Stern, E. A.; Newville, M.; Ravel, B.; Yacoby, Y.; Haskel, D. *Physica B* **1995**, *208−209*, 117.

(40) *X-Ray Absorption. Principles, Applications, Techniques of EXAFS, SEXAFS and XANES*; Prins, R., Koningsberger, D. C., Eds.; Wiley: New York, 1988.

(41) Tröger, L.; Yokoyama, T.; Arvanitis, D.; Lederer, T.; Tischer, M.; Baberschke, K. *Phys. Rev. B* **1994**, *49*, 888.

(42) Rehr, J. J.; Albers, R. C.; Zabinsky, S. I. *Phys. Rev. Lett.* **1992**, *69*, 3397.

(43) Clausen, B. S.; Grabaek, L.; Topsoe, H.; Hansen, L. B.; Stoltze, P.; Norskov, J. K.; Nielsen, O. H. *J. Catal.* **1993**, *141*, 368.

(44) Faupel, F. *Phys. Status Solidi A* **1992**, *134*, 9.

(45) Crank, J.; Park, C. S. *Diffusion in Polymers*; Academic Press: London, 1968.

(46) Bennett, M. R.; Wright, J. G. *Phys. Status Solidi A* **1972**, *13*, 135.

(47) Leung, P. K.; Wright, J. G. *Phil. Mag.* **1974**, *30*, 185.

(48) Wyckoff, R. W. G. *Crystal Structures*; R. E. Krieger: Malabar, Florida, 1982; Vol. 1.

(49) Gloor, A. P.; Prins, R. *J. Phys. Chem.* **1994**, *98*, 9865.

(50) Harada, M.; Asakura, K.; Toshima, N. *Jpn. J. Appl. Phys.* **1993**, Suppl. *32−2*, 451.

(51) Schmid, G.; Lehnert, A.; Malm, J.-O.; Bovin, J.-O. *Angew. Chem., Int. Ed. Engl.* **1991**, *30*, 874.

(52) Wicke, E.; Brodowsky, H. In *Hydrogen in Metals II*; Alefeld, G., Völkl, J., Eds.; Springer: Berlin, 1978.

(53) Peisl, H. In *Hydrogen in Metals I*; Alefeld, G., Völkl, G., Eds.; Springer: Berlin, 1978.

(54) *Binary Alloy Phase Diagrams*; Massalski, T. B., Okamoto, H., Subramanian, P. R., Kacprzak, L., Eds.; ASM International: Metals Park, OH, 1990; Vol. 1.

(55) Greegor, R. B.; Lytle, F. W. *J. Catal.* **1980**, *63*, 476.

(56) Montano, P. A.; Shenoy, G. K.; Alp, E. E.; Schulze, W.; Urban, J. *Phys. Rev. Lett.* **1986**, *56*, 2076.

(57) Kip, B. J.; Duivenvoorden, F. B. M.; Koningsberger, D. C.; Prins, R. *J. Catal.* **1987**, *105*, 26.

(58) Montano, P. A.; Zhao, J.; Ramanathan, M.; Shenoy, G. K.; Schulze, W.; Urban, J. *Chem. Phys. Lett.* **1989**, *164*, 126.

(59) Sankar, G.; Thomas, J. M.; Waller, D.; Couves, J. W.; Catlow, C. R. A.; Greaves, G. N. *J. Phys. Chem.* **1992**, *96*, 7485.

(60) Ashcroft, A. T.; Cheetham, A. K.; Harris, P. J. F.; Jones, R. H.; Natarajan, S.; Sankar, G.; Stedman, N. J.; Thomas, J. M. *Catal. Lett.* **1994**, *24*, 47.

(61) Benfield, R. E. *J. Chem. Soc., Faraday Trans.* **1992**, *88*, 1107.

(62) Fritsche, H.-G.; Benfield, R. E. *Suppl. Z. Phys. D* **1993**, *26*, 15.